PDIV Modelling for Rectangular Wire Turn-to-Turn Insulation of Inverter-Fed Motors through Thermal Ageing

H. Naderiallaf, M. Degano, *Senior Member, IEEE*, and C. Gerada, *Senior Member, IEEE*

***Abstract*— This contribution develops the partial discharge inception voltage (PDIV)-FEM-based model based on Schumann's streamer inception criterion (SCSIC) with respect to thermal ageing time (TAGT) or the insulation lifetime for the turn-to-turn insulation of coil winding made by rectangular insulated wires. The accelerated thermal ageing is performed at 250°C, which is 50°C higher than the thermal class, with ageing intervals of 156 and 312 hours. PDIV measurements are conducted at a constant temperature of 25°C, 40% relative humidity, and atmospheric pressure (1013 mbar). The measurements are done under AC 50 Hz excitations, following IEC 60034-18-41 guidelines for inverter-fed motor insulation system qualification. Furthermore, this study analyzes streamer inception parameters such as critical field line length (CFLL), effective ionization coefficient (α_{eff}), partial discharge (PD) inception field ($E_{discharge}$), firing voltage (V_{firing}) and its correlation with PD charge amplitude as a function of TAGT or the insulation lifetime.**

***Index Terms*— Accelerated ageing, inverter-fed machine, partial discharges, partial discharge inception voltage.**

NOMENCLATURE

B10	10th percentile
CFL	Critical field line
CFLL	Critical field line length
FEM	Finite element method
FL	Field line
FLL	Field line length
K	Schumann constant
PD	Partial discharge
PDIV	Partial discharge inception voltage
SCSIC	Schumann's streamer inception criterion
TAG	Thermal ageing
TAGT	Thermal ageing time

I. INTRODUCTION

THE automobiles' CO_2 emissions are regulated in each country yearly as the threat of global warming grows [1]. The automotive sectors have developed electrically-powered vehicles, including electric vehicles (EVs) and hybrid electric vehicles (HEVs), to reduce CO_2 emissions. Coil windings of traction motors in EVs and HEVs are made using rectangular insulated wires (e.g., edgewise wires) to achieve higher motor efficiency compared to randomly wound windings [2]. Fig. 1 illustrates typical coil windings manufactured using edgewise-insulated wires.

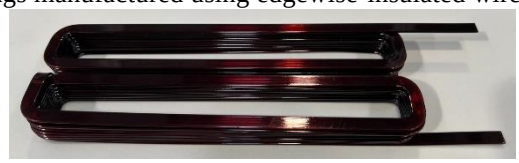

Fig 1. Typical coil windings formed from edgewise enamelled wires.

Indeed, to obtain high filling factors for decreased copper losses and higher power densities, rectangular wires have been introduced [3]. Additionally, inverter-fed motors use high dV/dt power converters to increase power density, imposing significant electrical stress on the winding turn-to-turn insulation in terms of partial discharge (PD) activity. Due to the greater insulation thickness and higher partial discharge inception voltage (PDIV), rectangular insulated wires are also preferable to custom round wires from this perspective. Moreover, since the wires' placement is more well-defined, managing the turn-to-turn voltage is easier than randomly wound winding.

Turn-to-turn insulation experiences the highest electrical stress because of interactions between power converters and coil windings [5], [6]. When the PD inception field is exceeded by the electric field corresponding to the turn-to-turn insulation, PD activity begins and accelerates insulation degradation, especially if the winding wires are only covered with organic insulation. In this condition, PD may lead to early failure and shorten the lifespan to a few days, if not hours [9]. Therefore, the PD-free criterion must be followed when designing inverter-fed machines with Type I insulation (i.e., organic-only insulating materials). By addressing the research gap in the modelling of PDIV as a function of TAGT or the insulation lifetime, this contribution aims to expand the PDIV model based on the finite element method (FEM) proposed in

This paper was submitted for review in May 2023. This work was supported by the Clean Sky 2 Joint Undertaking through the European Union's Horizon 2020 Research and Innovation Programme under Grant 807081. *(Corresponding author: Hadi Naderiallaf).*

Hadi Naderiallaf, Michele Degano, and Chris Gerada are with the Power Electronics and Machines and Control (PEMC) Research Group, the University of Nottingham, Nottingham, U.K.
(e-mail: Hadi.Naderiallaf@nottingham.ac.uk; Michele.Degano@nottingham.ac.uk; Chris.Gerada@nottingham.ac.uk)

[12] by considering the impact of ageing on the insulation thickness and permittivity for rectangular insulated wires, in particular, the edgewise wires. To achieve this result, the approach involves (a) accelerated thermal ageing of insulated wires, (b) measuring PDIV for unaged and thermally aged turn-to-turn specimens, (c) electric field simulation and ionization swarm parameters calculations for both unaged and thermally aged samples, (d) using SCSIC to determine N_{cr}, the threshold number of electrons in a Townsend avalanche representing the transition to streamer discharge, and (e) deriving the Schumann constant, K, which is the natural logarithm of N_{cr}, as a function of TAGT or insulation lifetime. Once K is determined based on insulation lifetime, it can be used to predict PDIV. Differently from the existing works such as [12], [13] and [14], where only a single steady K is used, this contribution proves that K should be introduced as a function of TAGT or the insulation lifetime to enhance the PDIV modelling prediction consequent to the insulation ageing. This refinement is crucial because relying on a single K parameter obtained from the unaged insulation results in an overestimation of PDIV after insulation degradation, influencing the initial PD-free design of the electrical machine's insulation system. By deriving the K equations as a function of insulation lifetime, this work supports the insulation designers to guarantee the PD-free design throughout the targeted lifetime. Another novelty of this contribution compared to the existing works is that this work presents a comprehensive analysis of streamer inception parameters (SIPs) such as critical field line length (CFLL), effective ionization coefficient (α_{eff}), partial discharge (PD) inception field ($E_{discharge}$), firing voltage (V_{firing}) and its correlation with PD charge magnitude as a function of TAGT or the insulation lifetime for better understanding the PD phenomenology consequent to the ageing.

II. Methodology

The correct value of K at different ageing levels must be determined based on experimental data for the samples which model the turn-to-turn winding insulation. In light of this, unaged and thermally aged specimens are used for PDIV tests. The test samples are introduced in the first of the following subsections. Next, approaches to measure wire geometry dimensions and the relative permittivity are described. The PDIV measuring setup and test method are then explained.

A. Test Samples

PDIV tests are performed on the pairs of edgewise enamelled wires wrapped in polytetrafluoroethylene (PTFE), modelling the turn-to-turn winding insulation system in electrical machines, Fig. 2. The base and topcoat of the wire insulation are polyester-imide and polyamide-imide, respectively, with a thermal class of 200°C. The measurements are accomplished for unaged and thermally aged samples to investigate the impact of TAG on the turn-to-turn insulation. The accelerated TAG of each wire is carried out at 250°C (i.e., 50°C higher than the thermal class) for two ageing periods:

Fig. 2. Edgewise insulated wires (top) before and (below) after wrapping in PTFE, test sample.

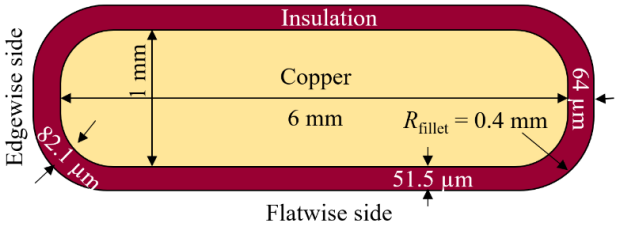

Fig. 3. Unaged edgewise insulated wire cross-section dimensions.

156 and 312 hours, before being wrapped with PTFE. The turn-to-turn winding insulation is assessed at two distinct levels of thermal degradation using these two ageing cycles. The "ten-degree" approach, which offers a rough approximation for insulation deterioration, is applied to select the ageing time based on [15]. This rule states that the lifespan of the insulation is halved for every 10°C increase in temperature above the thermal index (TI). In this instance, if the anticipated longevity of an insulation system at TI is 20,000 hours, the lifespan dramatically drops to about 625 hours when the temperature exceeds 250°C, which is 50°C higher than TI. Consequently, putting the insulation to accelerated thermal ageing at 250°C for 156 hours and 312 hours, respectively, equates to around 25% and 50% of the overall insulation lifetime.

B. Wire Geometry Dimensions and Relative Permittivity Measurements

The bare copper wire dimensions, insulation thicknesses (flatwise, edgewise and fillet sides), and fillet radius of the unaged edgewise enamelled wire are illustrated in Fig. 3. The wire cross-section dimensions (i.e., copper length and width, insulation thickness: flatwise and edgewise sides) are measured by a micrometre screw with an accuracy of 1 µm. The insulation thickness is calculated by differentiating the measured dimensions before and after stripping. The wires are stripped using a laser wire stripping device, ensuring only the insulation and not any copper is removed. For each group of unaged and thermally aged wires, 35 wires are considered to measure the required dimensions, and the averaged values are then recorded. Additionally, the fillet radius value, R_{fillet}, is equal to 0.4 mm provided by the wire manufacturer. The insulation thickness at the fillet side for unaged and thermally aged wires is interpolated using the sketch tools in COMSOL, considering the measured insulation thickness at flat and edgewise sides and assuming the fillet radius remains constant during the TAG.

Another input for the COMSOL model is the relative permittivity, determining the electric field distribution in the

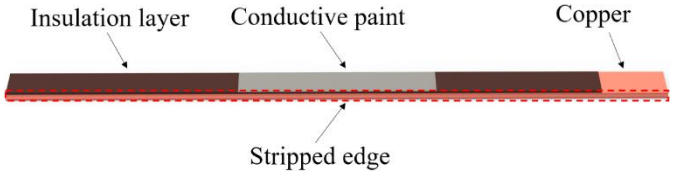

Fig. 4. Edge-stripped and painted rectangular wire.

electrostatic simulations. In order to measure the relative permittivity of a rectangular wire, the insulation part only at the edge sides of the edgewise wires are stripped. Therefore, the two square insulation layers at the top and bottom of the flat sides of the wires are separated. In order to build a planar capacitance, only one layer of insulation at the top or bottom of the flat sides is considered, and its middle is painted using a conductive paint for 5 cm to provide a ground electrode. In order to be able to energize the copper, only one side of the wire is also stripped. Fig. 4 shows the schematic of the prepared rectangular wire to measure capacitance and relative permittivity. Fig. 4 shows the portion of the wire's insulation that is painted using conductive paint to connect the live connection. In addition, the stripped edge of the wire is illustrated (the red dashed rectangular) where the insulation is removed to attain a planar capacitance, separating the upper and lower insulation layers of the wire.

The planar capacitance created between the wire copper and conductive paint is measured using a 50 Hz sinusoidal voltage waveform produced by a Megger Delta4000. The insulation capacitance is measured in steps of 20 V over the voltage range of 20 to 100 V at 25°C, and the averaged measured capacitance is recorded. The reason for selecting 25°C for the relative permittivity measurement is just to consider the same temperature as the used one for the PDIV tests. However, it is worthwhile to highlight that the relative permittivity variation is negligible up to the glass transition temperature (i.e., T_g) which is higher than 240°C for polyamide-imide. Indeed, the relative permittivity of polyamide-imide gets higher at temperature levels higher than T_g [16].

For each unaged and thermally aged wire level (i.e., aged for 156 and 312 hours at 250°C), 20 wires are used to be stripped and painted according to Fig. 4. The averaged measured apparent capacitance over 20 samples is considered to calculate the relative permittivity from (1):

$$\varepsilon_r = \frac{C_{\text{wire}} \cdot d_{\text{insul.}}}{\varepsilon_0 \cdot A} \quad (1)$$

where C_{wire} is the insulation layer capacitance in F, $d_{\text{insul.}}$ is the insulation thickness (flatwise) in m, ε_0 is the free space permittivity, and A is the insulation area covered by the conductive paint in m^2.

The average apparent capacitance for unaged and thermally aged insulation layers (i.e., aged for 156 and 312 hours) are 168.63, 210.65, and 222.91 pF, respectively. Eventually, the insulation thicknesses (flatwise, edgewise and fillet sides) and relative permittivity, which change as a function of TAGT, are inputs for the electrostatic simulations listed in Table I.

TABLE I
INSULATION THICKNESS AND RELATIVE PERMITTIVITY AS A FUNCTION OF TAGT

TAGT (h)	Insulation thickness (μm)			Relative permittivity
	Flatwise side	Edgewise side	Fillet side	
0	51.5	64	82.1	3.3
156	39	52.5	65.4	3.1
312	34.5	48.5	59.5	2.9

Table I presents the measured quantities, indicating a decrease in insulation thickness and permittivity due to thermal ageing. The reduction in insulation thickness is likely caused by polyamide-imide shrinkage or vaporization during thermal ageing. The decrease in permittivity can be attributed to the formation of more porous spaces in the insulation as it degrades. This leads to increased air encapsulation within the voids of the insulation material. As air has a permittivity close to one, which is lower than that of wire insulation, the overall permittivity is observed to decrease due to insulation deterioration [11].

C. PDIV Measurement Setup and Test Procedure

IEC 60034-18-41 [17] allows measuring PDIV under either sinusoidal or impulsive voltage excitations for the turn-to-turn insulation evaluation of inverter-fed motors. The measured PDIV using AC 50 Hz supply gives a conservative assessment for the turn-to-turn insulation under 2-level inverter or surge generator waveforms [8], [18], [19]. Indeed, the measured PDIV under AC 50 Hz excitation is lower than that of steep-fronted square waveform with a rise time shorter than 1 μs [20]. Thus, AC PDIV tests are conducted under sinusoidal waveform excitation at 50 Hz, providing conservative values for PDIV.

The AC source is GPT-9802, made by GW Instek. The applied voltage across the specimen is monitored by a Teledyne LeCroy WaveSurfer 510 oscilloscope (1 GHz bandwidth, 10 GS/s sampling rate) measured by a CT4079-NA differential probe (50 MHz bandwidth, 2000:1 voltage ratio, 50 Ω impendence). A conventional indirect circuit schematized in Fig. 5 is used to detect PD. A PD-free 1 nF coupling capacitor is connected in parallel with the test sample to increase the signal-to-noise ratio and improve the measurement sensitivity. The PD sensor is a ferrite-core high-frequency current transformer (HFCT) with 1-60 MHz bandwidth made by Techimp. The PD detection unit is a Techimp PD BaseII detector with an acquisition frequency range from 16 kHz to 48 MHz and a sampling rate of 200 MSa/s.

The tests are carried out at 25°C temperature, RH 40%, and at atmospheric pressure (1013 mbar) inside a test chamber with the ability to control temperature and humidity. Starting from a voltage level well below PDIV, the peak of applied voltage increases in steps of 10 V every 30 s. Once the PD is detected, the peak value of the voltage is recorded as PDIV. The PDIV measurements are accomplished using five unused test specimens corresponding to each ageing condition: pristine and thermally aged samples relevant to the two accelerated ageing periods: 156 and 312 hours.

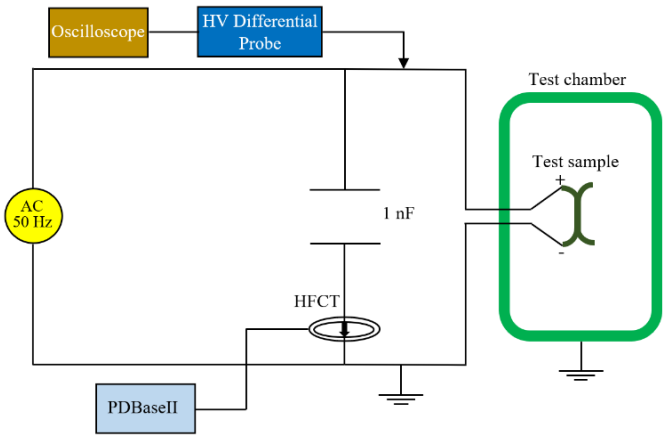

Fig. 5. PDIV measurement setup circuit and connections layout.

Each test specimen is tested only once to avoid the potential effects of past measures (such as a PDIV reduction due to prior discharge activities) [21]. Therefore, five unused samples are tested to create the set of data. The mean peak value of PDIV and B10 of the 2-parameter Weibull distribution are used to report the measured PDIV. Furthermore, the measurement results dispersion level is also analysed quantitatively, relying on the shape/slope parameter of the Weibull distribution (i.e., β).

III. SCSIC Implementation

K determines the earliest value of the critical number of carriers at the head of the avalanche, known as avalanche size, N_c, through an exponential function as (2) [22]. Indeed, when the avalanche size reaches a specified value of N_c, fast-moving filamentary streamers start to emanate from the head of the avalanche [23].

$$N_c = exp\,(K) \tag{2}$$

K is a dimensionless constant calculated from (3) based on SCSIC [22]:

$$K = \int_0^{x_c} \alpha_{eff}(x) \cdot dx \tag{3}$$

where x is the distance from the kick-off point of the avalanche where incepted by a single primary electron. x_c is the length of an avalanche's path along the electric FL where the earliest discharge event commences.

α_{eff} is the effective ionization coefficient of air characterized as:

$$\alpha_{eff} = \alpha - \eta \tag{4}$$

where α and η are gas ionization and the attachment coefficients, respectively, varying by gas type, electric field magnitude, and gas density, thus gas pressure [24].

It is assumed that the time between two subsequent PDIV measurements is sufficiently long so that the deposited charges caused by the previous test can decay or recombine. Therefore, air ionisation is the only way to start a discharge event [13].

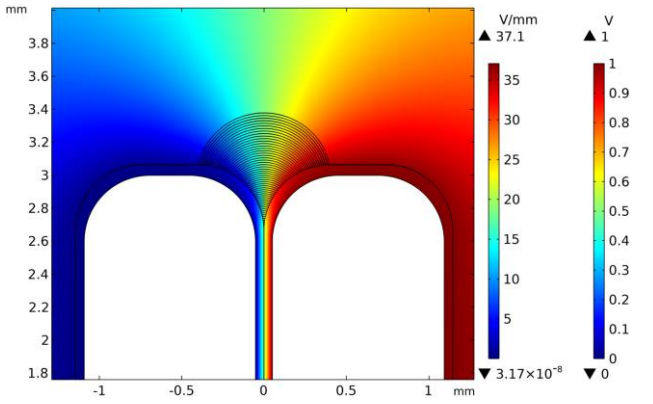

Fig. 6. Electric field distribution simulation between two rectangular insulated wires using a 2D COMSOL Multiphysics® [12].

Furthermore, to prevent the effects of space charge accumulation on both the field distribution in the air wedge and PDIV, bipolar excitations with polarity reversal (e.g., AC) are preferred to voltage waveforms with a DC component (e.g., unipolar excitations) [25].

A. Non-Uniform Electric Field Distribution Simulation

Using electrostatic computations, the two-dimensional (2D) axisymmetric model in COMSOL Multiphysics® simulates the non-uniform electric field distribution in the air wedge between two rectangular insulated wires based on FEM (Fig. 6).

Three simulations are performed for 1) unaged and thermally aged edgewise insulated wires for 2) 156 hours @ 250°C and 3) 312 hours @ 250°C, referring to the insulation thickness and relative permittivity, changing as a function of the TAGT, parametrized in Table I and the 2D wire's cross-section geometry of Fig. 3.

The primary electrostatic computations are conducted with a unitary voltage to acquire a reference database, [12], for unaged and thermally aged turn-to-turn insulation systems. A simulation output (i.e., reference database) includes: 1) only FLLs in the air wedge between the wires, arranged from shortest to longest, and 2) the electric field magnitudes associated with each FLs, having a decreasing trend subsequently. It is important to note that only the latter is increased with rising voltage which should be computed for each voltage level to update the reference database. However, the former (i.e., FLLs) remains constant with increasing voltage.

B. Deriving Ionization Swarm Parameters

The BOLSIG+ software uses the ionization swarm parameters introduced in the LXCAT database for dry air to determine the air ionization (α) and attachment (η) coefficients necessary in (4) [26], [27]. The inputs of BOLSIG+ are the range limit of the reduced electric field, E/n, in Townsend, at which the ionization swarm parameters should be calculated, the gas temperature in Kelvin, and the moist air composition in percentage (%). The minimum and maximum reduced electric

field, E/n, correspond to the longest and shortest FLLs, respectively, considered the computation range limit. E is the electric field in V/m relevant to each FL computed by COMSOL. n is the gas number density in m^{-3} which is given by the ideal gas law as (5):

$$n = p \cdot V/k_B \cdot T \quad (5)$$

where p is the gas pressure in Pascals, V is the test volume in m^3, k_B is the Boltzmann constant, $1.380649\times10^{-23}\ J/K$, and T is the gas absolute temperature in Kelvin.

The moist air composition relevant to the test conditions (i.e., relative humidity (RH) = 40%, T = 25°C, p = 1013 mbar) can be estimated from (6):

$$moist\ gas\ ratio\ (x) = dry\ gas\ ratio\ (x) \cdot (1 - M_{H_2O}) \quad (6)$$

where x is the gas in the air composition, including Nitrogen (N_2), Oxygen (O_2), Argon (Ar), and carbon dioxide (CO_2). The dry gas ratio corresponding to each of these gases in the air composition is reported in [28] at room temperature (20°C), such as 78.08% N_2, 20.95% O_2, 0.93% Ar, and 0.04% CO_2. M_{H_2O} in (6) is the water molar concentration in air derived by [13]:

$$M_{H_2O} = 0.622 \cdot \left(\frac{p_{H_2O}}{p - p_{H_2O}}\right) \quad (7)$$

where 0.622 is the ratio between the molar masses of water (18.02) to that of air (28.96). p_{H_2O} is the vapour pressure of water in Pascals, calculated from the empirical equation (8) [13]:

$$p_{H_2O} = 611 \cdot RH \cdot 10^{7.5\left(\frac{t_{amb}}{t_{amb+237}}\right)} \quad (8)$$

where RH and t_{amb} are relative humidity and gas temperature in °C, respectively. Therefore, Table II summarizes the defined gas compositions of moist air relevant to the test conditions derived from (6) to (8) as inputs for BOLSIG+. Finally, BOLSIG+ gives α/n and η/n both in m^2 as a function of the reduced electric field, E/n, in Townsend, as outputs.

TABLE II
GAS COMPOSITIONS OF MOIST AIR IN PERCENTAGE (%)

Ar	CO_2	H_2O	N_2	O_2
0.92	0.04	0.8	77.46	20.78

C. K Calculation Algorithm under PDIV

The following algorithm [12] is developed in MATLAB to determine the experimental value of K corresponding to unaged and thermally aged turn-to-turn insulation samples:

1) Import COMSOL output: FLLs in mm vs electric field magnitude in V/m simulated with unitary voltage.

2) Update only the electric field intensity across each FL in step 1) by linearity considering the measured peak value of PDIV (e.g., $PDIV_{mean}$ or $PDIV_{B10}$) from (9):

$$E(x,y) = PDIV \cdot E_{database}(x.y) \quad (9)$$

3) Import BOLSIG+ output and use (4) to introduce α_{eff}/n in m^2 vs reduced electric field, E/n, in Townsend.

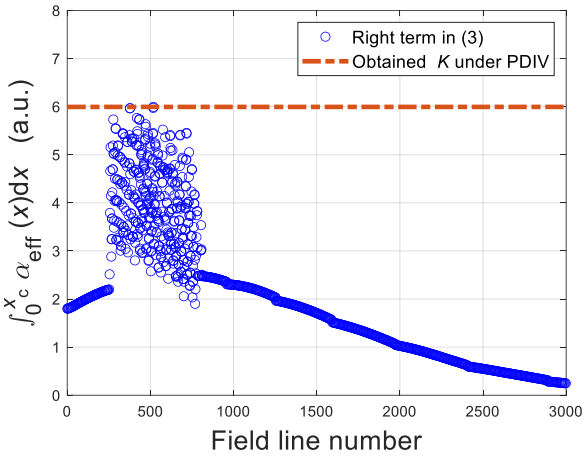

Fig. 7. Visualization of the method for determining the maximum value of the right term in (3) as K in the SCSIC algorithm for estimating PDIV.

3-1 Unit conversion of E/n in Townsend to electric field in V/m:

$$E(V/m) = n \cdot Townsend \cdot 10^{-21} \quad (10)$$

3-2 Unit conversion of α_{eff}/n in m^2 to α_{eff} in mm^{-1}:

$$\alpha_{eff}(mm^{-1}) = n \cdot \alpha_{eff}/n \cdot 10^{-3} \quad (11)$$

4) For each FL, derive α_{eff} in mm^{-1} from the imported database in step 3), considering the FL electric field intensity under PDIV, step 2).

5) Compute the right term in (3) for all the FL numbers, n_{FL}.

6) Report the highest K calculated in step 5), as illustrated in Fig. 7, as the experimental value of K that is used in the SCSIC to estimate PDIV. The FLL along which the maximum value of K is delivered is recorded as CFLL.

In Fig. 7, the FLs are sorted and numbered from the shortest to the longest, corresponding to the highest and lowest electric field strength, respectively. It is evident from Fig. 7 that a critical region or swollen area exists for α_{eff}, consequently, for the right term in (3). Within this region, the dispersion of α_{eff} experiences a significant increase at a particular field line number or electric field strength. This critical region plays a decisive role in determining the CFL and its corresponding α_{eff}, as the maximum value of the right term in (3), thus K, is always found in this region.

IV. RESULTS AND DISCUSSIONS

A. Measured PDIV

In Fig. 8, the measured PDIV values are presented, showing both the "mean" and the "10th percentile of PDIV" (i.e., B10). The latter is obtained by fitting the measured PDIV data to the 2-parameter Weibull distribution. Fig. 8 shows the PDIV reduction consequent to TAGT as expected. $PDIV_{mean}$ and $PDIV_{B10}$ diminish by 17.4% and 21.5%, respectively, after 312 hours of ageing at 250°C. This PDIV drop is most likely due to the insulation thickness shrinking during the accelerated TAG

process (Fig. 9). In addition, the difference between $PDIV_{mean}$ and $PDIV_{B10}$ increases with the ageing time, manifesting a higher PDIV dispersion vs ageing period (Fig. 10).

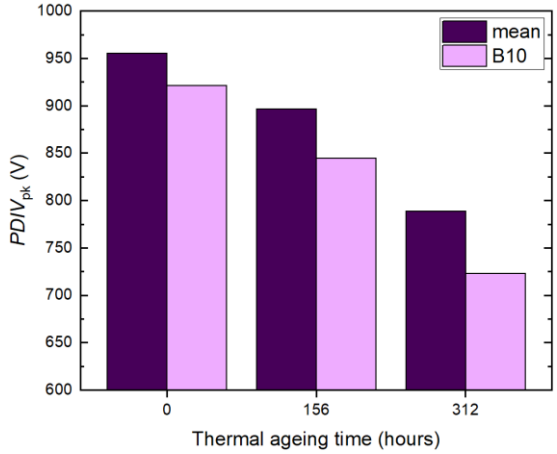

Fig. 8. Measured PDIV peak under AC 50 Hz excitation as a function of TAGT.

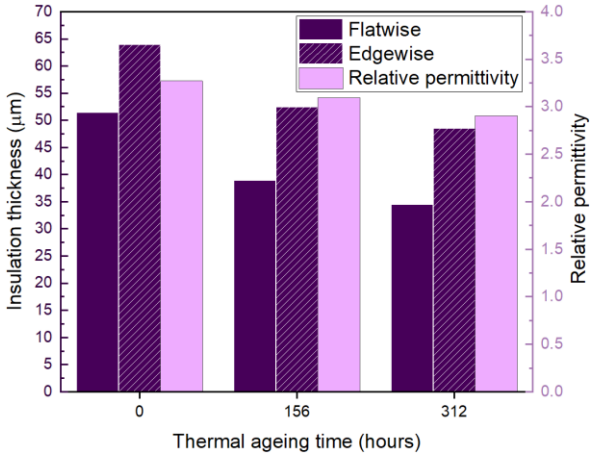

Fig. 9. Insulation thickness (flatwise and edgewise sides) and relative permittivity as a function of TAGT.

B. Insulation Thickness and Relative Permittivity

Fig. 9 illustrates the insulation thickness shrinking (flatwise and edgewise sides) and relative permittivity reduction as a function of the TAGT. While the former leads to a decrease in PDIV, the opposite effect holds for the latter, where a lower relative permittivity can result in a lower electric field intensity in the air and, consequently, a higher PDIV. Since PDIV reduces vs TAGT, it is concluded that the impact of a smaller insulation thickness on PDIV predominates over the effect of relative permittivity reduction on PDIV. The insulation thickness reduction rate is slightly higher for the edgewise side than the flatwise one. For example, it shrank by about 33% and 24.2% for the edgewise and flatwise sides, respectively, after 312 hours of ageing. However, the rate of relative permittivity reduction consequent to TAG is lower than that of insulation thickness shrinking, where relative permittivity becomes 88.7% of the unaged insulation after 312 hours of ageing. The slight reduction of relative permittivity consequent to the TAG can be ascribed to either or both (a) polar compounds vaporization, which has a higher relative permittivity than the insulation (e.g., moisture) and (b) air ingression in the porous aged insulation, which has a lower relative permittivity than the insulation. As a result, the thermally aged insulation can become dried and brittle, delivering a lower relative permittivity than the unaged insulation.

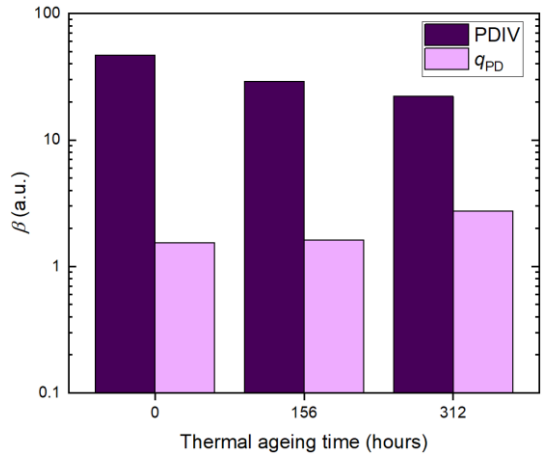

Fig. 10. Dispersion level of PDIV and PD charge amplitude under AC 50 Hz excitation as a function of TAGT.

C. PDIV and PD Charge Amplitude Dispersion Level

Fig. 10 quantifies the dispersion level of the measured PDIV peak and PD charge amplitude, q_{PD}, under PDIV as a function of TAGT, relying on the shape/slope parameter of the 2-parameter Weibull distribution (i.e., β). Fig. 10 displays the opposite trends of the dispersion level of these two parameters (i.e., β of PDIV and q_{PD}) vs TAGT. Indeed, while β of PDIV decreases (i.e., PDIV dispersion increases), β of q_{PD} increases (i.e., q_{PD} dispersion decreases) with ageing. As a result, these two parameters (i.e., β of PDIV and q_{PD}) can be considered ageing indicators for the edgewise enamelled wire.

Regarding the β of q_{PD}, it is noteworthy to highlight that it becomes larger than 2 (i.e., $2 < \beta < 4.8$) [29] after 312 hours of TAG, probably manifesting more contribution for internal PD occurrence due to the insulation delamination caused by the TAG process. However, the opposite stands for β of q_{PD} before 312 hours, where it is smaller than two (i.e., $\beta < 2$), indicating a more possibility for the PD activity between the turn-to-turn insulation (i.e., in the air wedge between the insulated wires).

D. CFLL

Fig. 11 represents the CFLL variations as a function of the TAGT. It should be mentioned that all the CFLs are found between the fillet sides of the two wires. In other words, the maximum value of K under PDIV at atmospheric pressure (i.e., 1013 mbar) is always found in the air wedge between the fillet sides of the wires. Therefore, it is not necessary to consider the external FLs (i.e., beyond the fillet side) at atmospheric pressure. Fig. 11 shows that the CFLL obtained from $PDIV_{mean}$ shortens monotone with the TAGT while it is always higher than that obtained from $PDIV_{B10}$. In addition, CFLL always

remains below the insulation thickness at the fillet side. For instance, considering the obtained value from $PDIV_{mean}$, the ratio of CFLL to the insulation thickness at the fillet side is 77%, 85%, and 80% for unaged samples, and thermally aged ones for 156 and 312 hours, respectively, manifesting an average value of 80.7% throughout the TAGT.

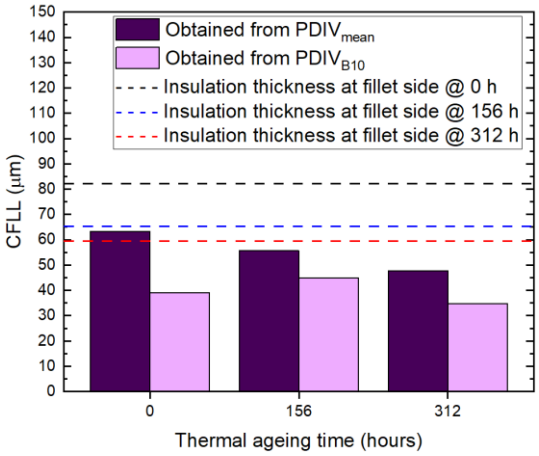

Fig. 11. CFLL as a function of TAGT obtained from $PDIV_{mean}$ and $PDIV_{B10}$. (The dashed black, blue, and red lines indicate the insulation thickness at the fillet side for unaged (0 h), and thermally aged samples for 156 and 312 hours, respectively).

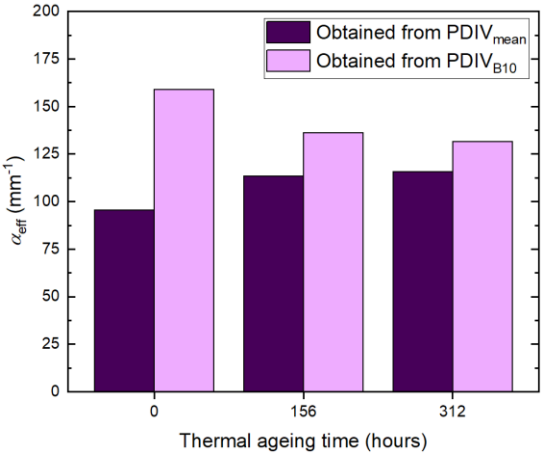

Fig. 12. α_{eff} across the CFLL as a function of TAGT obtained from $PDIV_{mean}$ and $PDIV_{B10}$.

E. Effective Ionization Coefficient of Air

Fig. 12 shows the values of effective ionization of air (α_{eff}) corresponding to the CFLL for unaged and thermally aged samples derived from $PDIV_{mean}$ and $PDIV_{B10}$. As illustrated in Fig. 12, the obtained α_{eff} from $PDIV_{B10}$ is higher than that obtained from $PDIV_{mean}$ which is the opposite of the case for CFLL (Fig. 11). The observed result can be attributed to a stronger electric field across a smaller CFL, as seen in Fig. 13. Indeed, the probability of air ionization increases as the CFLL gets shorter because the electric field strength throughout its length increases (Fig. 13). Consequently, as shown in Fig. 12, α_{eff} obtained from $PDIV_{B10}$ is higher than that derived from $PDIV_{mean}$. Conversely, the opposite holds true for the CFLL, as depicted in Fig. 11. In addition, it is interesting that α_{eff} for the thermally aged samples remains almost stable equal to 114.6 and 133.9 mm^{-1} from $PDIV_{mean}$ and $PDIV_{B10}$, respectively.

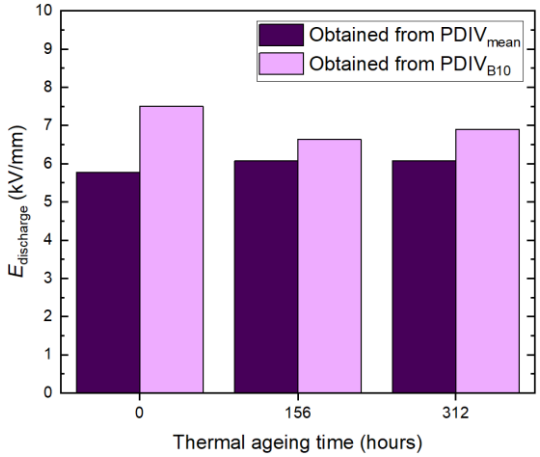

Fig. 13. Discharge electric field as a function of TAGT obtained from $PDIV_{mean}$ and $PDIV_{B10}$.

F. Discharge Electric Field

Fig. 13 displays the values of discharge electric field ($E_{discharge}$) relevant to the CFLLs reported in Fig. 11 for unaged and thermally aged samples obtained from $PDIV_{mean}$ and $PDIV_{B10}$. Like α_{eff}, the intensity of $E_{discharge}$ obtained from $PDIV_{B10}$ is more than that of $PDIV_{mean}$. Furthermore, $E_{discharge}$ obtained from $PDIV_{mean}$ for the thermally aged specimens is almost constant at 6.1 kV/mm.

G. Firing Voltage

Fig. 14 indicates variations of firing voltage as a function of TAGT. The firing voltage across the CFL, V_{firing}, is determined by the multiplication of $E_{discharge}$ (reported in Fig. 13) by its correspondent CFLL (quantified in Fig. 11).

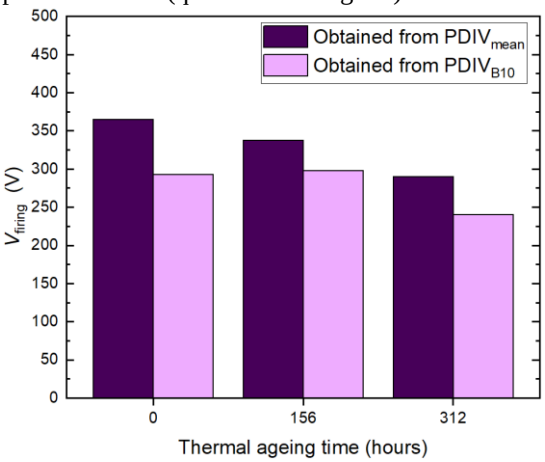

Fig. 14. Firing voltage as a function of TAGT obtained from $PDIV_{mean}$ and $PDIV_{B10}$.

As shown in Fig. 14, the obtained V_{firing} from $PDIV_{mean}$ is higher than that of $PDIV_{B10}$ similar to the trend observed for CFLL. Based on $PDIV_{mean}$, V_{firing} weakens with increasing TAGT, decreasing from 364.9 to 290.1 V. Since there is a

relationship between PD charge amplitude and V_{firing}, [29], the correlation plot between $Q_{\text{max,95\%}}$ (95$^{\text{th}}$ percentile of PD charge amplitudes fitted to the Weibull distribution) and V_{firing}, normalized to unaged mean, is depicted in Fig. 15, showing that as V_{firing} decreases, PD charge amplitude also decreases.

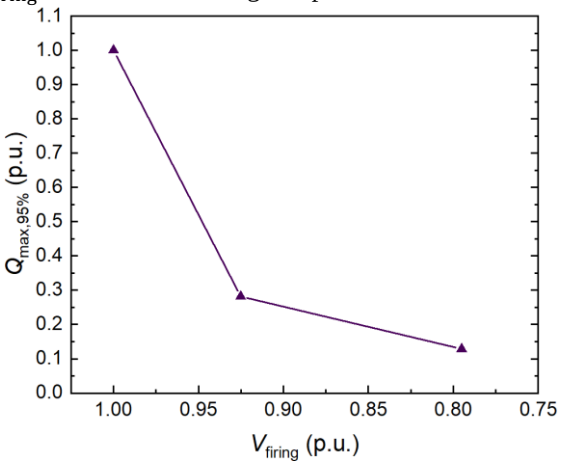

Fig. 15. The correlation plot between firing voltage and $Q_{\text{max,95\%}}$, normalized to unaged mean.

H. Schumann Constant (K)

Fig. 16 reports the calculated value of K as a function of TAG based on the $\text{PDIV}_{\text{mean}}$ and PDIV_{B10}. As shown in Fig. 16, there is an almost stable K value ($K \approx 6.17$) for unaged and thermally aged samples for 156 hours (i.e., approximately 25% of insulation lifetime) which is very useful for PDIV modelling. However, K is slightly lower for the thermally aged samples for 312 hours (i.e., approximately 50% of insulation lifetime), equal to 5.52 and 4.57 obtained from the $\text{PDIV}_{\text{mean}}$ and PDIV_{B10}, respectively. Additionally, the difference between the obtained K from the $\text{PDIV}_{\text{mean}}$ and PDIV_{B10} is higher for the thermally aged samples for the most prolonged period (i.e., 312 hours), which can be ascribed to the highest PDIV dispersion for these specimens (Fig. 10).

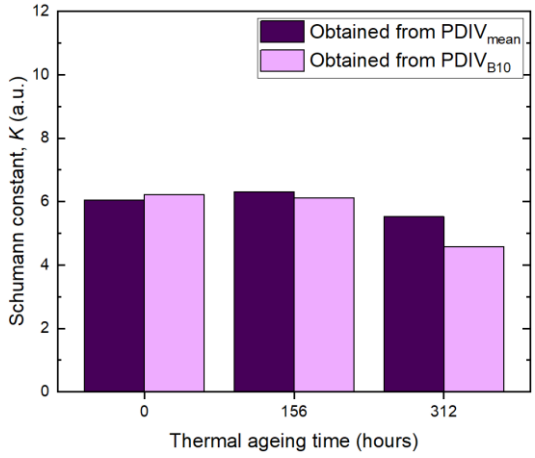

Fig. 16. Variations of K as a function of TAGT obtained from $\text{PDIV}_{\text{mean}}$ and PDIV_{B10}.

The reason for a lower K value at 312 hours can be attributed to the used approach for K calculation. Considering SCSIC, the first assumption is that the discharge event occurs only at the air wedge between the wires, and the insulation is void-free. However, as already observed from β of q_{PD} at 312 hours (i.e., $\beta > 2$) (Fig. 10), there is a possibility of internal PD in voids or delamination resulting from the ageing. Thus, since the portion of FLL only in the air wedge between the wires is considered to calculate K, a lower K value at 312 hours (i.e., approximately 50% of insulation lifetime) is achieved compared with those of unaged and thermally aged specimens for 156 hours (i.e., approximately 25% of insulation lifetime). As a result, using the introduced approach and reaching a lower K value than 6.17 at atmospheric pressure (i.e., 1013 mbar) can be considered as an indicator for internal PD activities, thus delamination/void creation, for the turn-to-turn insulation of inverter-fed motors. Based on this theory, the cavity depth or delamination height can be estimated from (12):

$$h_{\text{defect,312h}} = \frac{K_{\text{unaged}} - K_{\text{312h}}}{\alpha_{\text{eff,312h}}} \tag{12}$$

where $h_{\text{defect,312h}}$ is the approximated defect height (e.g., cavity depth or delamination height) after 312 hours of TAG. K_{unaged} and K_{312h} are the Schumann constants for unaged and thermally aged samples for 312 hours, respectively. $\alpha_{\text{eff,312h}}$ is the effective ionization coefficient of air corresponding to the CFL at 312 hours which is equal to 115.63 and 131.5 mm^{-1} obtained from $\text{PDIV}_{\text{mean}}$ and PDIV_{B10}, respectively. Therefore, the estimated defect height at 312 hours is obtained equal to 4.4 and 12.5 µm based on $\text{PDIV}_{\text{mean}}$ and PDIV_{B10}, respectively, from (12).

It is possible to derive regression line equations fitted to K as a function of t, which is the accelerated TAGT at 250°C:

$$K_{\text{mean}}(t) = -0.0016 \cdot t + 6.2119 \tag{13}$$

$$K_{\text{B10}}(t) = -0.0053 \cdot t + 6.4588 \tag{14}$$

where $K_{\text{mean}}(t)$ and $K_{\text{B10}}(t)$ are representing K as a function of t obtained from $\text{PDIV}_{\text{mean}}$ and PDIV_{B10}, respectively. The coefficient of determinations, R^2, for (13) and (14) are equal to 0.41 and 0.8, respectively. This shows that (14) is more reliable than (13), predicting 80% of the variance in K with respect to t. It is worth noting that the parameter "t" in equations (13) and (14) can be approximated as the insulation lifetime based on the "ten-degree" rule [15]. For instance, 156 and 312 hours at 250°C are roughly equivalent to 25% and 50% of the insulation lifetime, respectively.

V. PDIV Modelling Based on SCSIC

Considering the obtained K values reported in Fig. 16, along with the derived K equations (i.e., (13) and (14)), the PDIV prediction is now possible up to 50% of the insulation lifetime. Fig. 17 shows a flowchart summarizing the iterative approach to model PDIV.

The iterative algorithm is used to predict PDIV, [12], as a function of TAGT at 250°C, and it follows these steps:

1) Choose one of the following values for K as required:

1-1 $K = 5.956$: Average value of K relevant to unaged and thermally aged samples for 156 and 312 hours obtained from $PDIV_{mean}$.

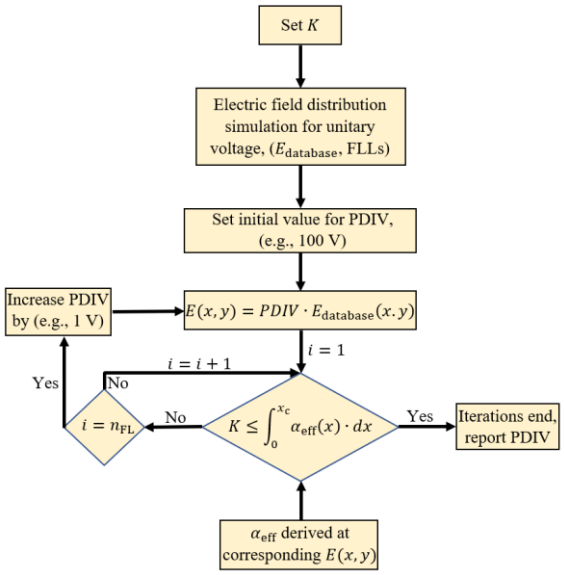

Fig. 17. Flowchart depicting the iterative approach for modeling PDIV.

1-2 $K = 5.637$: Average value of K relevant to unaged and thermally aged samples for 156 and 312 hours obtained from $PDIV_{B10}$.

1-3 $K_{mean}(t)$: Represented by (13)

1-4 $K_{B10}(t)$: Represented by (14)

2) Import the electric field distribution by COMSOL for unitary voltage (i.e., 1 V) as a database. Consider an initial arbitrary value for PDIV e.g., 100 V.

3) Compute the electric field magnitude across each FL in the air wedge between the two insulated wires for the selected voltage level (as shown in Fig. 6) by linearity from (9).

4) Import the database of the effective ionization coefficient of air from BOLSIG+, representing α_{eff} as a function of the electric field.

5) Scan the FL from the shortest to the longest, checking all the FL numbers, n_{FL}, to determine if, for at least one FL, $K \leq \int_0^{x_c} \alpha_{eff}(x) \cdot dx$ is satisfied. If not, increase the applied voltage (e.g., by 1 V) and go back to step 3 to find PDIV.

6) The termination condition for the iteration process is when $K \leq \int_0^{x_c} \alpha_{eff}(x) \cdot dx$ is assured. Once this condition is satisfied, cease the iteration, and declare the applied voltage as the predicted PDIV.

Fig. 18 presents the ratio of modelled and measured PDIV as a function of TAGT, considering the four K values listed in stage 1) of the PDIV predictive algorithm. Additionally, Table III reports the PDIV estimation results, quantifying the prediction errors in percentage (%). Overall, all the proposed K values provide reasonable predictions of $PDIV_{mean}$ and $PDIV_{B10}$ within a confidence interval of 90%, demonstrating a very high accuracy. Table III indicates that the maximum error is 8.85% which is attributed to $PDIV_{mean}$ estimation for unaged samples using $K = 5.956$.

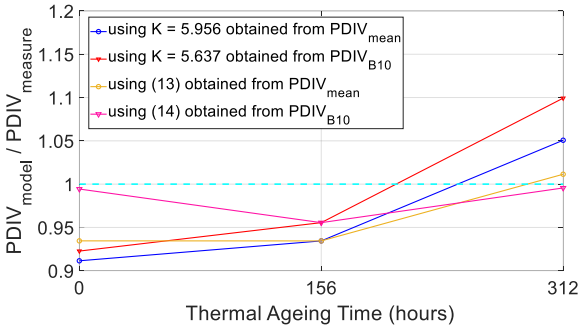

Fig. 18. The ratio of modelled and measured PDIV as a function of TAGT.

TABLE III
MODELLED $PDIV_{PK}$ VS MEASURED $PDIV_{PK}$

TAGT (h)	Measured $PDIV_{pk}$ (V)		K (a.u.)	Modelled $PDIV_{pk}$ (V)	Error (%)
0	Mean	955.6	5.956	871	-8.85
			(13)	893	-6.55
	B10	921.2	5.637	850	-7.73
			(14)	916	-0.56
156	Mean	896.8	5.956	838	-6.56
			(13)	838	-6.56
	B10	844.5	5.637	807	-4.45
			(14)	807	-4.45
312	Mean	789	5.956	829	5.07
			(13)	798	1.14
	B10	723.2	5.637	795	9.93
			(14)	720	-0.44

Fig. 18 substantiates that the introduced K equation based on B10 of PDIV (14) predicts $PDIV_{B10}$ with the highest accuracy compared with other K values considering unaged and thermally aged samples. For example, Table III shows that the lowest error is achieved when (14) is used to predict $PDIV_{B10}$, manifesting 0.44% and 0.56% error for thermally aged specimens for 312 h and unaged ones, respectively. For unaged turn-to-turn insulation, the modelled PDIV based on (13) and (14) deliver better accuracy than the predicted PDIV using the simple average value of K. This is more evident when the intention is to predict $PDIV_{B10}$ where using (14) delivers almost 14 times lower error compared to the case when $K = 5.637$ is used. Regarding the aged samples for 156 hours, there is no difference between using K equations or the average value of K to predict PDIV, while referring to B10 of PDIV gives better accuracy to anticipate PDIV with an error of 4.45%. Considering the aged specimens for 312 hours, while the average value of K obtained from $PDIV_{B10}$ delivers less accuracy (i.e., 10% overestimation), the modelled B10 of PDIV from (14) provides conservative PDIV with the highest accuracy (0.44% error). Thus, for a turn-to-turn insulation which has passed half of its lifetime (i.e., thermally aged for 312 h, at 250°C), referring to (14) to estimate $PDIV_{B10}$ gives about 23 times lower error compared to the case when $K = 5.637$ is employed. It is worthwhile to highlight that ageing can impact the model accuracy if a single parameter of K is used. But as suggested in this contribution, if K is introduced as a function of thermal ageing time (i.e., insulation lifetime), then the proposed model based on SCSIC can still be used with

esteemed reliability and accuracy. The introduction of K as a function of TAGT or insulation lifetime significantly improves the accuracy of PDIV prediction when using SCSIC for thermally aged specimens, as shown in Fig. 18 and Table III. Indeed, this approach calculates K considering only the air wedge between wires. However, as depicted in Fig. 16, K can vary with TAGT or insulation lifetime due to insulation delamination, leading to lower K values when turn-to-turn insulations are aged. Thus, deriving K equations based on ageing time or insulation lifetime becomes essential to enhance the model accuracy after insulation ageing.

VI. Conclusion

This contribution presents a PDIV model based on SCSIC for the turn-to-turn insulation of coil windings, particularly edgewise wires, under thermal ageing conditions. The model takes into account the effects of insulation thickness shrinking and relative permittivity reduction due to the ageing process. It is demonstrated that by deriving K equations based on ageing time or insulation lifetime, the model accuracy increases conspicuously after insulation ageing. The study also explores other streamer inception parameters, such as CFLL, effective ionization coefficient of air, discharge electric field, and firing voltage, as functions of TAGT. The model reveals a correlation between firing voltage and PD charge amplitude with increasing TAGT. Considering the impact of TAG on PDIV, which is a critical stress element on turn-to-turn insulation in inverter-fed motors for automotive applications, the developed PDIV model provides valuable support to coil winding designers in designing more reliable systems when using rectangular insulated wires. The fast and accurate prediction capabilities of the model allow designers to make informed design choices without relying solely on extensive experimental campaigns. This enhancement in prediction accuracy ensures safer and more reliable coil winding designs in automotive applications.

References

[1] C. Li, Y. Yang, G. Xu, Y. Zhou, M. Jia, S. Zhong, Y. Gao, C. Park, Q. Liu, Y. Wang, and S. Akram, “Insulating materials for realising carbon neutrality: Opportunities, remaining issues and challenges,” *High Voltage*, vol. 7, no. 4, pp. 610-632, 2022.

[2] T. Wakimoto, H. Kojima, and N. Hayakawa, “Measurement and evaluation of partial discharge inception voltage for enamelled rectangular wires under AC voltage,” *IEEE Trans. Dielectr. Electr. Insul.*, vol. 23, no. 6, pp. 3566-3574, Dec. 2016.

[3] T. Okada, H. Matsumori, T. Kosaka, and N. Matsui, “Hybrid excitation flux switching motor with permanent magnet placed at middle of field coil slots and high filling factor windings,” *CES Trans. Electr. Mach. Syst.*, vol. 3, no. 3, pp. 248-258, Sept. 2019.

[4] Y. Zhao, D. Li, T. Pei, and R. Qu, “Overview of the rectangular wire windings AC electrical machine,” *CES Trans. Electr. Mach. Syst.*, vol. 3, no. 2, pp. 160-169, June 2019.

[5] E. Persson, “Transient effects in application of PWM inverters to induction motors,” in *Proc. Conf. Rec. Annu. Pulp Paper Ind. Tech. Conf.*, Jun. 1991, pp. 228-233.

[6] M. Melfi, A. M. J. Sung, S. Bell, and G. L. Skibinski, “Effect of surge voltage risetime on the insulation of low-voltage machines fed by PWM converters,” *IEEE Trans. Ind. Appl.*, vol. 34, no. 4, pp. 766-775, Jul. 1998.

[7] L. Lusuardi, A. Rumi, A. Cavallini, D. Barater, and S. Nuzzo, “Partial discharge phenomena in electrical machines for the more electrical aircraft. Part II: impact of reduced pressures and wide bandgap devices,” *IEEE Access*, vol. 9, pp. 27485-27495, 2021.

[8] A. Rumi, L. Lusuardi, A. Cavallini, M. Pastura, D. Barater, and S. Nuzzo, “Partial Discharges in Electrical Machines for the More Electrical Aircraft. Part III: Preventing Partial Discharges,” *IEEE Access*, vol. 9, pp. 30113-30123, 2021.

[9] A. Cavallini, D. Fabiani, and G. C. Montanari, “Power electronics and electrical insulation systems - part 2: life modeling for insulation design,” *IEEE Electr. Insul. Mag.*, vol. 26, no. 4, pp. 33-39, Jul-Aug. 2010.

[10] IEC Std. 60034-18-41, “Rotating electrical machines - part 18-41: partial discharge free electrical insulation systems (Type I) used in rotating electrical machines fed from voltage converters - qualification and quality control tests,” 2019.

[11] H. Naderiallaf, P. Giangrande, and M. Galea, “A contribution to thermal ageing assessment of Glass fibre insulated wire based on partial discharges activity,” *IEEE Access*, vol. 10, pp. 41186-41200, 2022.

[12] L. Lusuardi, A. Cavallini, M. G. de la Calle, J. M. Martínez-Tarifa, and G. Robles, “Insulation design of low voltage electrical motors fed by PWM inverters,” *IEEE Electr. Insul. Mag.*, vol. 35, no. 3, pp. 7-15, May-Jun. 2019.

[13] L. Lusuardi, “Towards a partial discharge free insulation system for the More Electrical Transportation,” Ph.D. dissertation, University of Bologna, Bologna, Italy, Mar. 2020.

[14] J. Gao, A. Rumi, Y. He and A. Cavallini, “Towards a holistic approach to inverter-fed machine design: FEM-based PDIV prediction of complete windings,” *IEEE Transactions on Dielectrics and Electrical Insulation*, June 2023.

[15] IEEE Std 117-2015 (Revision of IEEE Std 117-1974), *IEEE Standard Test Procedure for Thermal Evaluation of Systems of Insulating Materials for Random-Wound AC Electric Machinery*, vol., no., pp. 1-34, May 6, 2016.

[16] A. Rumi, J. Marinelli, and A. Cavallini, “Dielectric characterization of impregnating varnishes for inverter-fed motors,” in *2022 IEEE 4th International Conference on Dielectrics (ICD)*, Palermo, Italy, 2022, pp. 389-392.

[17] IEC Std. 60034-18-41, “Rotating electrical machines - part 18-41: partial discharge free electrical insulation systems (Type I) used in rotating electrical machines fed from voltage converters - qualification and quality control tests,” 2019.

[18] A. Rumi, J. G. Marinelli, A. Cavallini, and P. Seri, “Can corona resistant wires ensure reliability in aerospace machine insulation?,” in *2022 IEEE Electrical Insulation Conference (EIC)*, Knoxville, TN, USA, 2022, pp. 309-312.

[19] G. C. Montanari and P. Seri, “About the definition of PDIV and RPDIV in designing insulation systems for rotating machines controlled by inverters,” in *2018 IEEE Electrical Insulation Conference (EIC)*, 2018, pp. 554-557.

[20] C. Abadie, “On-line non-intrusive partial discharge detection in aeronautical systems,” Ph.D. dissertation, University of Toulouse, 2017.

[21] M. Goldman, A. Goldman, and J. Gatellet, “Physical and chemical aspects of partial discharges and their effects on materials,” in *1993 International Conference on Partial Discharge*, 1993, pp. 11-14.

[22] W. O. Schumann, “Über das Minimum der Durchbruchfeldstärke bei Kugelelektroden,” *Arch. Elektrotech. (Berl.)*, vol. 12, pp. 593-608, 1923.

[23] H. Raether, “Electron avalanches and breakdown in gases,” *Butterworth and Co. Publishers Ltd.*, 1964.

[24] N. H. Malik, “Streamer breakdown criterion for compressed gases,” *IEEE Trans. Electr. Insul.*, vol. EI-16, no. 5, pp. 463-467, Oct. 1981.

[25] H. Naderiallaf, P. Giangrande, and M. Galea, “Characterization of PDIV, PDEV, and RPDIV in insulated wires under unipolar repetitive square wave excitations for inverter-fed motors,” *IEEE Access*, vol. 11, pp. 51047-51063, 2023.

[26] G. J. M. Hagelaar and L. C. Pitchford, “Solving the Boltzmann equation to obtain electron transport coefficients and rate coefficients for fluid models,” *Plasma Sources Sci. Technol.*, vol. 14, no. 4, pp. 722-733, 2005.

[27] “BOLSIG+ | Electron Boltzmann equation solver.” [Online]. Available: http://www.bolsig.laplace.univ-tlse.fr/. [Accessed: Mar. 20, 2023].

[28] U.S. Committee on Extension to the Standard Atmosphere, “US Standard Atmosphere,” National Oceanic and Atmospheric Administration, 1976.

[29] P. Seri, H. Naderiallaf, and G. C. Montanari, “Modelling of supply voltage frequency effect on partial discharge repetition rate and charge amplitude from AC to DC at room temperature,” *IEEE Trans. Dielec. Electr. Insul.*, vol. 27, no. 3, pp. 764-772, June 2020.